Title

P-wave velocity anisotropy related to sealed fractures reactivation tracing the structural diagenesis in carbonates

Authors

Matonti, C
Guglielmi, Y
Viseur, S
et al.

Publication Date

2017-05-01

DOI

10.1016/j.tecto.2017.03.019

Peer reviewed

P-wave velocity anisotropy related to sealed fractures reactivation tracing the structural diagenesis in carbonates

Author links open overlay panel C.Matonti[ab] Y.Guglielmi[ac] S.Viseur[a] S.Garambois[d] L.Marié[a]
Show more

https://doi.org/10.1016/j.tecto.2017.03.019 Get rights and content

Highlights

- V_p measured on a meter scale block affected by reactivated and non-reactivated fractures
- Fracture reactivation decreases V_p and leads to dip anisotropy of about 10%.
- It is explained by the diagenetic evolution of fracture infilling material.
- Karstification is only a second-order cause, amplifying pre-existing anisotropy.

Abstract

Fracture properties are important in carbonate reservoir characterization, as they are responsible for a large part of the fluid transfer properties at all scales. It is especially true in tight rocks where the matrix transfer properties only slightly contribute to the fluid flow. Open fractures are known to strongly affect seismic velocities, amplitudes and anisotropy. Here, we explore the impact of fracture evolution on the geophysical signature and directional V_p anisotropy of fractured carbonates through diagenesis.
For that purpose, we studied a meter-scale, parallelepiped quarry block of limestone using a detailed structural and diagenetic characterization, and numerous V_p measurements. The block is affected by two *en-échelon* fracture clusters, both being formed in opening mode (mode 1) and cemented, but only one being reactivated in shear. We compared the diagenetic evolution of the fractures, which are almost all 100% filled with successive calcitecements, with the P-wave velocities measured across this meter-scale block of carbonate, which recorded the tectonic and diagenetic changes of a South Provence sedimentary basin.
We found that a directional V_p anisotropy magnitude as high as 8–16% correlates with the reactivated fractures' cluster dip angle, which is explained by the complex filling sequence and softer material present inside the fractures that have been reactivated

during the basin's tectonic inversion. We show that although a late karstification phase preferentially affected these reactivated fractures, it only amplified the pre-existing anisotropy due to tectonic shear. We conclude that V_p anisotropy measurements may help to identify the fracture sealing/opening processes associated with polyphased tectonic history, the anisotropy being independent of the current stress-state. This case shows that velocity anisotropies induced by fractures resulted here from a cause that is different from how these features have often been interpreted: selective reactivation of sealed fractures clusters rather than direction of currently open ones.

Graphical abstract

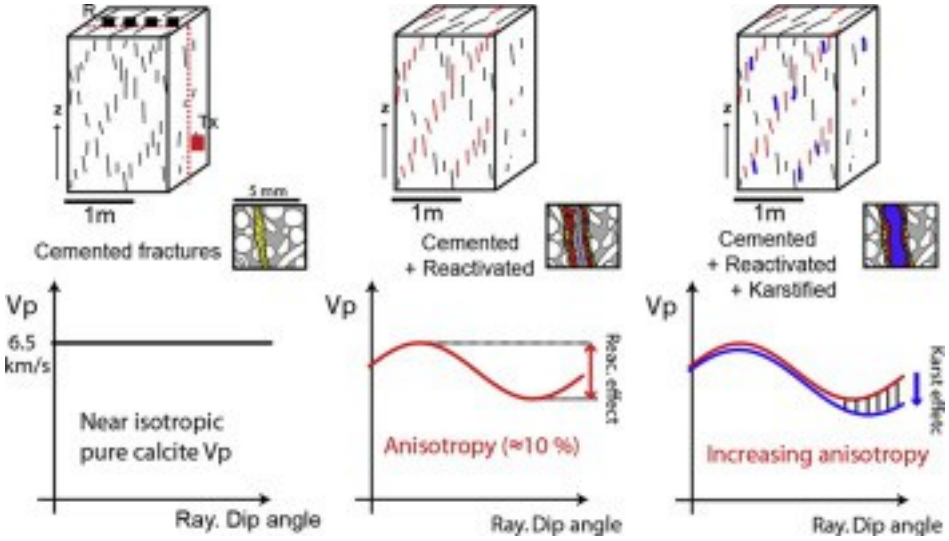

1. Download high-res image (112KB)
2. Download full-size image

- **Previous** article in issue
- **Next** article in issue

Keywords

Fracture diagenesis
Sealing
Reactivation
P-wave velocity
Anisotropy
Subseismic scale

1. Introduction

Fractures are responsible for a large part of the rock's fluid transfer properties, especially in unconventional (tight) reservoirs, but flow occurs only where fractures are not sealed with cement. Cemented fractures (and partially cement-filled fractures) are widespread in the subsurface (e.g., Aguilera, 1998, Laubach, 2003, Nelson, 2001). Borehole logging and core data indicate that in many cases it is the degree of fracture cementation rather than the fracture orientation (with respect to the stress tensor) that limits the fluid flow in the reservoirs and crust (Laubach et al., 2004). The amount of cement filling the fractures modulates the fractures' apertures, and, in turn, their hydraulic conductivity. It also modifies the fractures' elastic properties and their response to stress (Laubach et al., 2010, Lavenu et al., 2014). This concept explains why fluid flow may exist in fractures at great depths of several kilometers, even when confining pressure is high, and acts a primary contributor to constrain fluids migrations. Indeed, cement bridges within fractures increase resistance to closure at depth (Gale et al., 2010, Laubach et al., 2004).

To remotely explore the effects of fractures on rock properties, one approach is to correlate fracture spacing or properties to the anisotropy of mechanical wave velocity or amplitude variations with offset (or azimuth). This phenomenon is caused at seismic frequencies by the preferred alignment of open fractures (e.g. Queen and Rizer, 1990, Rüger and Tsvankin, 1997, Ali and Worthington, 2011). In addition, spacing and compliance of decametric fractures can, in theory, be inferred from scattered seismic waves generated by fractured layers (e.g., Fang et al., 2014, Zheng et al., 2013). However, in reservoirs, fractures are often assumed to remain open and to be more compliant, only if they are sub-parallel to the currently applied maximum principal stress direction. Another limitation is that, due to the seismic wavelengths, the structures relevant for evaluating fluid flow are often scaled below the current seismic resolution (15 to 20 m). Another way to remotely study fractures at adequate scale is by measuring shear wave splitting that fractured rocks can yield locally in borehole acoustic logs, or more recently in 3Dseismic data (e.g., Crampin and Lovell, 1991, Vetri et al., 2003, Prioul and Jocker, 2009).

However, in interpreting seismic anisotropy, only the effect of stress on fracture aperture is usually considered, neglecting the effects of natural fracture infilling material (Sayers et al., 2009). Indeed, many laboratory studies are performed on synthetic and/or single fractured samples that exhibit velocity and amplitude anisotropy sensitivity to the fracture compliance, size, mechanical aperture, fluid content and incidence angle of the wave (Leucci and De Giorgi, 2006, Moos and Zoback, 1983, Pyrak-Nolte et al., 1990a, Rathore et al., 1995, Schubnel and Guéguen, 2003). Laubach et al. (2004) also

demonstrated that open and permeable fractures can have any orientation, even perpendicular, with respect to the maximum horizontal stress.

Most laboratory studies that explore the links between acoustic velocity anisotropy and fracture properties usually consider fractures as two separate surfaces that match together more or less well (depending on the surface roughness), while the complex microstructural attributes of fractures are seldom considered. Therefore, studying the links between the microstructural attributes of natural fractures that undergo structural diagenesis, and acoustic wave propagation is rarely conducted, although such studies can provide useful information on the fractures crack-seal processes through time (Laubach et al., 2010, Gratier et al., 2013, Petit et al., 1999). Because cement precipitation is known to be sensitive to rock burial and thermal history, the degree of fracture cementation can be expected to evolve in a fairly predictable way for a given fracture network (Laubach and Diaz-Tushman, 2009) and might leave a trace on velocity anisotropy.

Here, we study densely fractured and non-porous pure carbonates. We focus on the complex diagenetic history of the fractures, which are characterized by alternate cementation, shear strain, and karstification phases. We propose to decipher the impact of fracture diagenetic and tectonic evolution on the current P-wave velocity measured through a meter-scale quarry block (Fig. 1, Fig. 2). This scale is of particular interest, being below the common seismic resolution, and above the possible rock sampling scales. Structural analysis of fractures at the meter-to-micrometer scale first indicates that the dense mode 1 cemented fractures network led initially to isotropic high P-wave velocity. We then demonstrate how successive fractures reactivation episodes induced P-wave velocity anisotropy in the studied rock block and how such anisotropy can help to discriminate the concurrent sealing/opening processes acting upon the fractures. We finally propose a timing of the structural diagenesis processes, we discuss which of these processes predominantly alters the acoustic properties of fractures, and then we highlight how variations of the velocity anisotropy could help to detect and assess these changes.

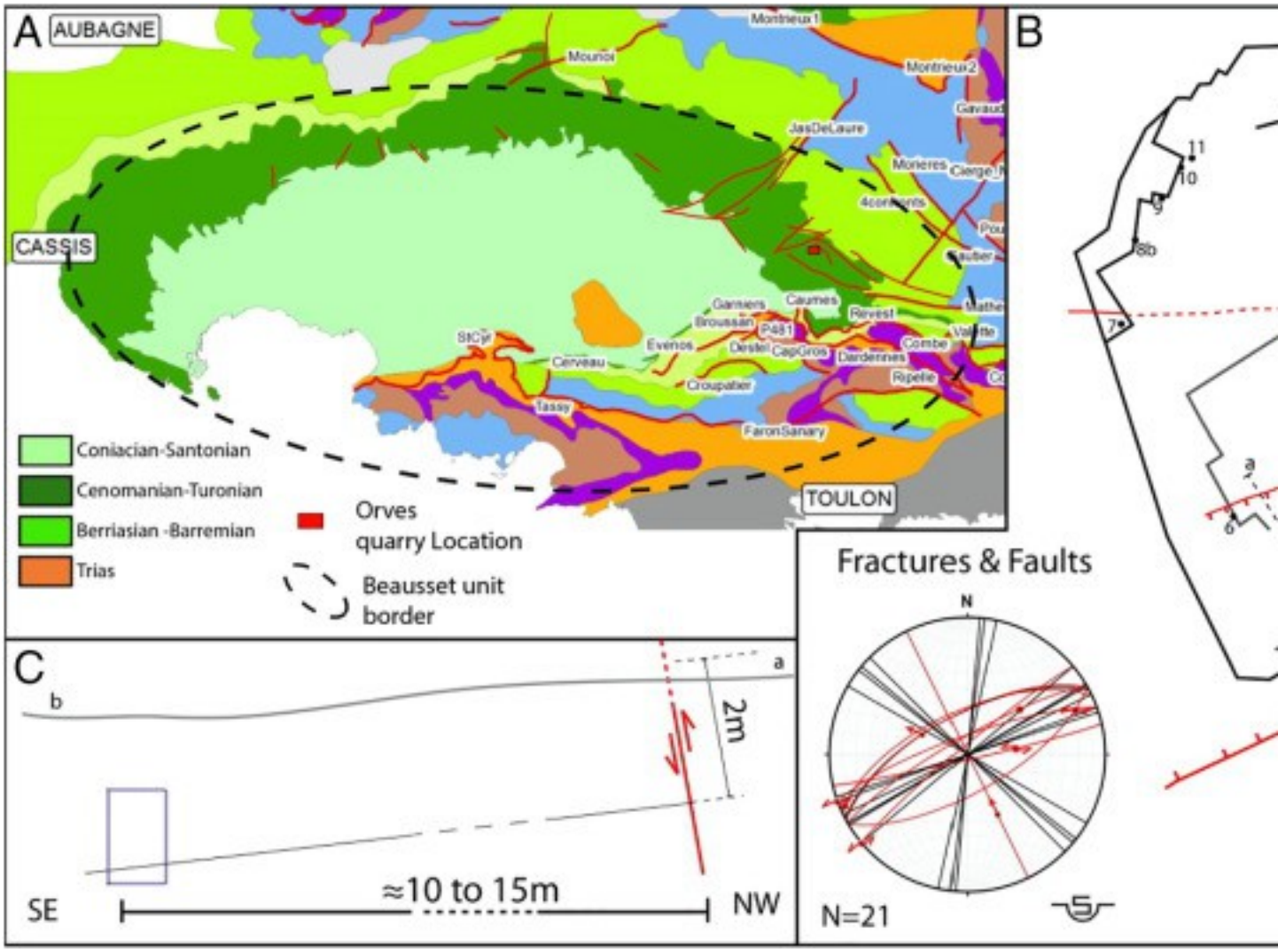

1. Download high-res image (380KB)
2. Download full-size image

Fig. 1. A: Simplified Geological Map at 1/50000 scale of the Beausset basin (modified from Fournillon, 2012) indicating the Orves quarry location. B: Structural map of the studied quarry showing the several polyphased faults affecting the rocks. (Lower left corner) stereogram of the fractures sets (in black) and faults (in red) in the quarry. C: Schematic cross section showing the block distance to the closest fault and its vertical offset.

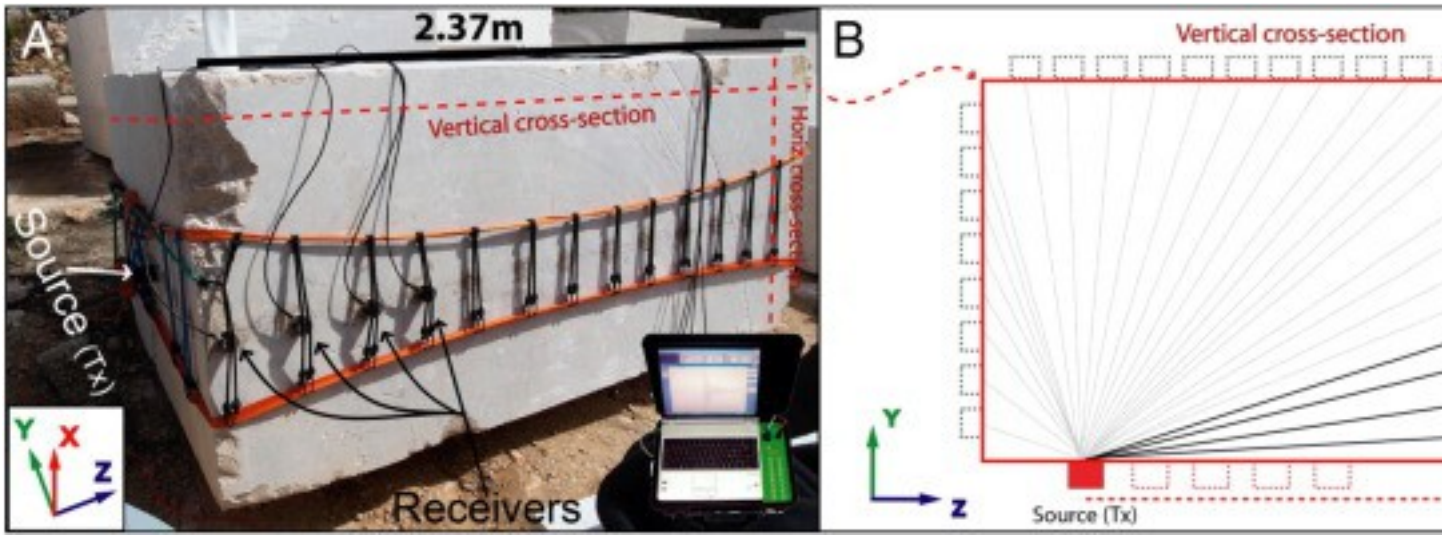

1. Download high-res image (261KB)
2. Download full-size image

Fig. 2. A Setting and acquisition apparatus of the P-wave velocity measurements. The source/receiver positions showed in the photograph are for illustration, the red dashed lines are the actual positions of the 2 geophysical cross-section performed 15 cm below block's faces. (The studied block is tip over the ground with vertical direction pointing to the right.); B: Geometry of source/receiver locations of the vertical ultrasonic cross-section.

2. Protocol

The investigated block is a 2.37 m × 1.51 m × 1.1 m parallelepiped made of limestone, extracted from the Orves quarry located in Southeast France (Fig. 1A). It displays a very regular shape due to the quarry extraction using a wire saw. A structural study of the block, along with thin section analyses of the fractures infilling materials, was performed first using an optical microscope (× 40 to 80) in cross-polarized light and then under cathodoluminescence in order to separate the different precipitation/dissolution phases. Seven porosity measurements were performed on one-inch long and one-inch diameter plugs using a helium porosimeter. These plugs were cored from the quarry wall in the same bed/interval where the block has been extracted.

P-wave velocity measurements were performed on the block using a TDAS-16 device (Boviar SRL; Fig. 2A). This apparatus includes an ultrasonic P-wave source (with a 55 kHz peak frequency) using a piezoelectric transducer. Transmitted signals through the rock were acquired simultaneously and sampled at a 1 MHz rate via four receivers. Receivers were positioned at different offsets, and moved at each measurement step around the three block faces away from the source (Fig. 2B). When all the receiver

positions had been used, the source was moved onto the next position, and so on, until all the block's faces were investigated (Fig. 2B). The separation distance between successive locations of the sources and receivers (i.e., each raypath ends) is 9 cm. The receivers were tightly attached to the block using textile straps and luggage elastics (Fig. 2A).

A total of 1826 ultrasonic velocity measurements were performed on two geophysical cross-sections, located respectively along the vertical ZY plane (1298 measurements) and the horizontal XY plane (528 measurements) (red dashed line in Fig. 2A). The two ultrasonic cross-sections were both located at 15 cm below, respectively, the block front vertical and upper horizontal faces (Fig. 2A). For the horizontal cross section, as the block lay tilted on the ground, only three faces were available to place the source and receivers, resulting in less ray angle coverage. In order to increase the signal/noise ratio, each velocity measurement was composed of at least 30 stacked successive pulses signals, and a coupling gel was set between the sensors and the rock surface to increase the signal amplitude. First arrival time picking was manually performed for each measurement with an accuracy of 0.001 ms. Stacking errors due to the time picking precision (± 0.001 ms) and to the accuracy of source-receiver distance determinations (± 4 cm) result in an average error lower than ± 2.5% on the P-wave velocity estimation. All the block structural features (cemented fractures, stylolites, and karstified fractures) were digitalized from high-resolution photographs (Fig. 3A and C) and imported into a Gocad software database. The fracture traces were represented as polylines (Fig. 3C and D) and relocated on each block's faces to reproduce their effective 3D location. To correlate the acoustic velocities to the block fracture's pattern geometry, an algorithm was developed to automatically compute the number of cemented fractures (in red in Fig. 4) intersecting each measurement raypath.

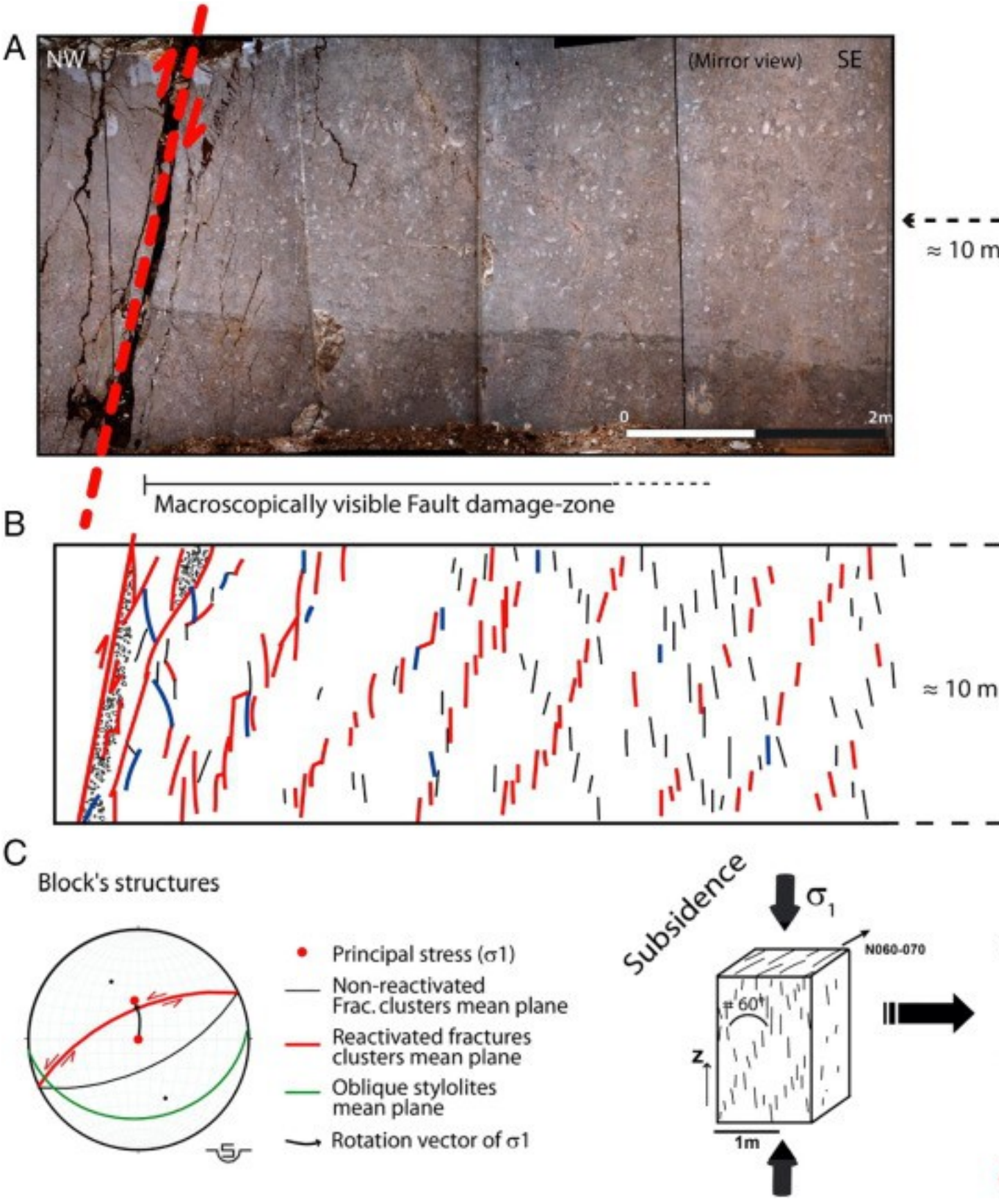
A
NW
(Mirror view)
SE
≈ 10 m
0
2m
Macroscopically visible Fault damage-zone
B
≈ 10 m
C
Block's structures
Principal stress (σ1)
Non-reactivated Frac. clusters mean plane
Reactivated fractures clusters mean plane
Oblique stylolites mean plane
Rotation vector of σ1
Subsidence
σ1
N060-070
60°
z
1m

1. Download high-res image (702KB)
2. Download full-size image

Fig. 3. A: Photographs of the quarry wall showing the rock interval where the block was extracted and his relative position from the closest fault in the quarry (photo of the outcrop is presented in mirror view in order to show the same orientation than the block); B: Scheme representation of the deformations and fracture pattern near (in the fault-zone) and far from faults, showing that the block fracture pattern is unaffected/not influenced by the fault zones; B: (left) stereogram of the 2 *en échelon* fractures clusters affecting the block (reactivated cluster in red, non-reactivated in black) outlining the rotation of the principal stress direction favoring the reactivation of one of the *en-échelon* fracture cluster (dipping W). (right) Sketches of the block showing the fracture pattern and the reactivation of the 55°W dipping fractures cluster that happened at the basin inversion; D–E histograms of fractures vertical trace lengths and fractures strike observed on the studied block.

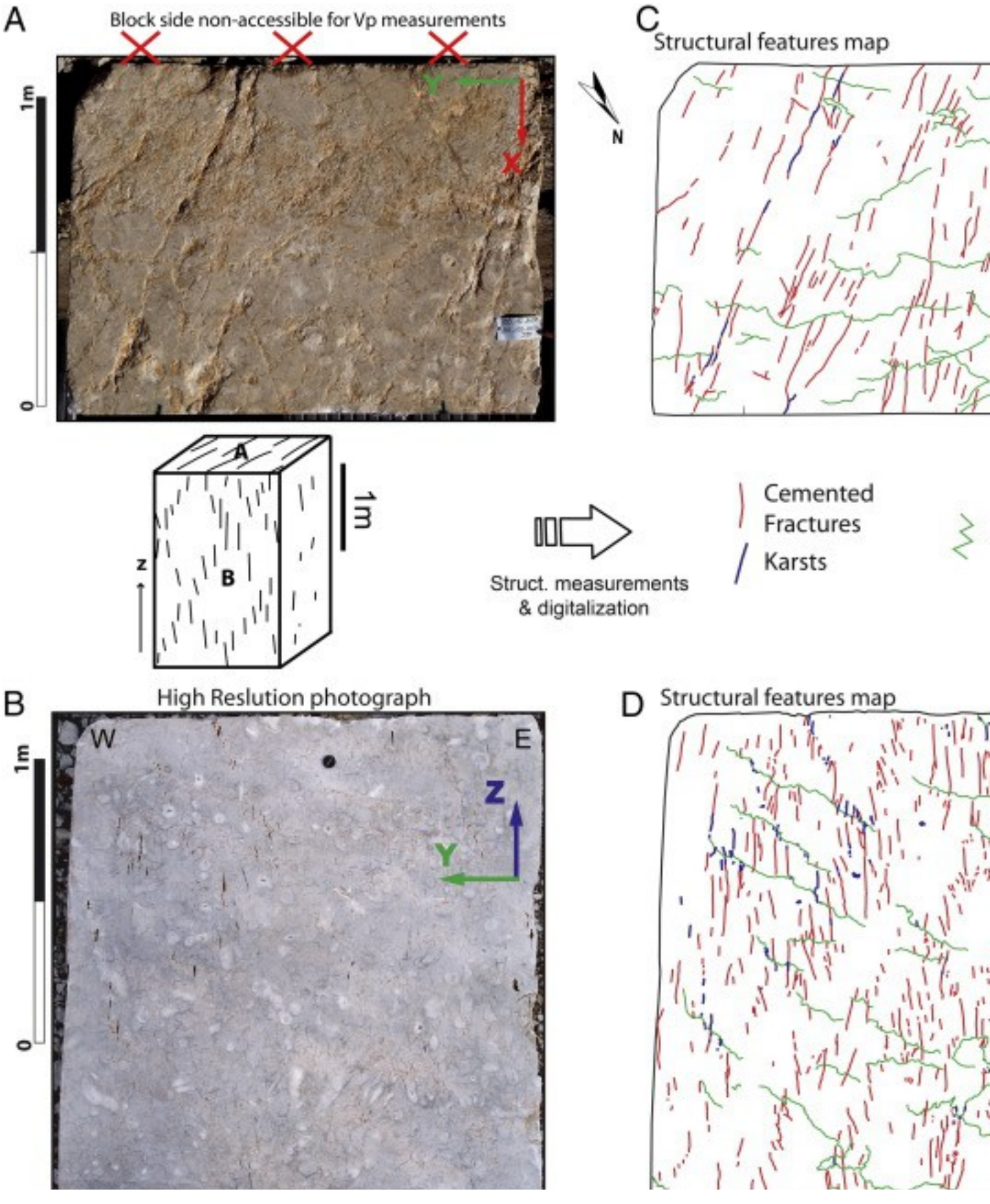
A
Block side non-accessible for Vp measurements
1m
0
Y
X
C
Structural features map
N
A
1m
Z
B
Struct. measurements
& digitalization
Cemented
Fractures
Karsts
B
High Reslution photograph
1m
0
W
E
Z
Y
D
Structural features map

1. Download high-res image (2MB)
2. Download full-size image

Fig. 4. A and C: High resolution photograph and structural map of the upper horizontal block face indicating which block side was not available for geophysical measurements; B and D: High resolution photograph and structural map of the vertical block face, showing the signification of the θ angle ranging between 0 and 180° (angle toward the vertical Z axis).

Our velocity analyses consider raypaths as straight lines. However, in heterogeneous media, mechanical waves are known to propagate along curved rays following the Fermat principle, due to multiple refractions of the waves when they cross media exhibiting velocity contrasts. To take into account the impact of curved raypaths on the computed P-wave velocity, we first performed a tomographic inversion of picked arrival times using a Simultaneous Iterative Reconstruction Technique (SIRT, Dines and Lyttle, 1979) on the vertical ultrasonic cross-section. We used a 10 cm grid, which provided more realistic shapes and lengths to the raypaths (RMS = 0.029; cf. Fig. 8, Fig. A1). Next, we recomputed V_p using these new curved raypath lengths and picked arrival times. It appears that in our case V_p calculated from curved rays deviate only by 11 m/s on average, i.e., < 0.2% (the maximum velocity discrepancy is 21 m/s), from those computed considering straight-line rays.

3. Geology and structure

3.1. Geological and structural context of the block's quarry

The studied block's quarry is located in the “Beausset” sedimentary Basin (southeast France) near its northeast border (Fig. 1A). This basin was filled with a > 2 km-thick pile of carbonate platform and slope deposits accumulated during successive tectonic subsidenceepisodes that occurred since the end of the Paleozoic, mainly during the late Cretaceoustranstensive tectonic phase (Turonian to Campanian, Hennuy, 2003, Philip, 1998). The Beausset Basin underwent successive compressive tectonic phases, the first being the basin inversion by the Pyrenean compression from the end of the Late Cretaceous to Eocene (e.g., Leleu, 2005). This compression led to the development of westward WNW-ESE thrusts, which now form the northeastern border of the basin, and to the exhumationand karstification of Cretaceous carbonate rocks. The second, the Alpine compression, started during the Miocene. However this tectonic compression has been determined to be responsible for < 10% of the total Provence rock tectonic shortening (Bestani et al., 2016).

The studied quarry is composed of Late to Terminal Cenomanian limestone exhibiting inner-platform, rudist-rich facies, forming successive meters-thick small emersive cycles. This sedimentary succession is overlaid by a surface accounting for both an emersion and then a marine erosion surface, which is overlaid by nodular argillaceous limestone and marls from early Turonian age. This erosion surface is characterized by a slight local angular unconformity, around 3°, compared to the Cenomanian limestones bedding dip.

Three fracture sets occur in the quarry, striking in average N000, N065 and N130 (Fig. 1B). These directions are compatible with Riedel structures (Riedel, 1929), respectively representing the R′, R and P directions, and relate well to the E/W transtensive basin scale's stress regime during the Turonian (Floquet and Hennuy, 2003). Several N060 to N070 faults cross through the quarry; their fault movements are polyphased. Microstructural markers analyses (stereogram in Fig. 1B) indicate that first faults were formed with a normal dip slipmovement, associated with striae around 70° pitch. This first movement is compatible with the slight angular unconformity observed between the top of the inner-platform carbonate rocks and the overlying Turonian marly deposits. This unconformity is likely related to a slight block rotation between newly formed normal faults, as we observe in the quarry (Fig. 1B), and marks the drowning of the Cenomanian carbonate platform in the Beausset basin (Floquet et al., 2013, Matonti, 2015). Then, these faults were reactivated in a strike-slip movement, and are associated with sub-horizontal 10 to 20° pitch striae, which is compatible with the Late Cretaceous to Eocene tectonic inversion characterized by a N/S compression.

The studied block was extracted approximately between 10 and 20 m from one of the faults which exhibits a vertical metric offset (Figs. 1C and 2A). This fault (N070; 80°W) displays a fault-zone that is classically composed of a fault core and a damage zone (e.g., Billi et al., 2003). The fault core is made of a continuous 10-to-20 cm thick chaotic breccia (sensu Mort and Woodcock, 2008), containing heterometric (cm to dm size) angular clasts from the host rock. The damaged zone, from 2.5° m toward the fault plane, displays high fracture density and shows an increase in fracture length from dm to ≤ 1 m, an increase in connectivity and in karstification/aperture, which is associated with increased shear slip on the pre-existing mode 1 fractures (Fig. 3A and B). However, no macroscopically discernible “fault-enhanced” strain markers are visible beyond 6 m to the fault plane (Fig. 3A and B). Outside this fault-zone the fractures pattern is mainly composed of two conjugate, *en-échelon*, cemented fracture clusters, similar to the fracture pattern exhibited in the studied block. Indeed the studied block was extracted outside of this fault zone's width (> 10 m).

3.2. Block geology and evidence of fracture reactivation

In the studied block, the sedimentary microfacies is characterized by a rich rudist fauna (mainly Radiolitidae in “life position”), embedded in a non-porous wackestone to packstone matrix (helium porosity always < 1.5%) that contains mostly micritized rudist shell clasts, benthic foraminifera, echinoderm clasts and peloïds. Only the N065 fracture set affects the block. This set is composed of two *en-échelon* clusters with different dips, around 55°E and 55°W (which respectively correspond to θ = 35° and θ = 145°, in Figs. 3C and 4B and D). These clusters form an angle in good accordance with the conjugate fractures model (Figs. 3A and 4B) (Anderson, 1951), suggesting they formed under a vertical principal stress σ_1, related to the basin opening (pre-inversion) paleo-stress regime (Fig. 3C). The *en-échelon*fractures forming the two clusters are subvertical and formed in tensile mode 1 (in red in Fig. 4C and D). At the time they formed, they could be considered as syntaxial calcite veins (sensu Bons et al., 2012). They exhibit kinematic/mechanical apertures (distance between fracture walls) mostly between 1 and 2 mm with maximum aperture of 9 mm. However, almost all of these fractures are completely sealed by calcite cement, thus making them non-permeable. They are elongated elliptic-shaped, with an average vertical length (height) of 10 cm and a horizontal length of up to 70 cm (Fig. 3D and in red in Fig. 4C). Both fracture clusters show comparable fracture densities, but only the cluster dipping 55°W (or θ = 145° in Fig. 3A–C), underwent a sinistral oblique-slip reactivation with a thrust component. This reactivation is related to the formation of oblique tectonic closed stylolite planes, dipping 45°E, i.e., sub-perpendicular to the 55°W reactivated fracture cluster (in green in Fig. 4D). These stylolites indicate change in the direction of the principal σ_1 stress during the fracture reactivation, which has been determined from the perpendicular (the pole) of the mean tectonic stylolites plane (green arc in Fig. 3C). That fracture reactivation is likely related to the reactivation of the N065 faults, and to the Basin tectonic inversion at the end of the Cretaceous, which is associated with a rotation of the principal stress vector (Fig. 3C). Fracture reactivation is observable from millimeters-to-centimeter offsets affecting some rudist shells along the 55°W cluster's fracture planes, which also appear slightly longer and wider than the non-reactivated 55°E dipping cluster's fractures. Moreover, the reactivated fractures always crosscut and offset the mode 1 non-reactivated ones (Fig. 5A). Locally, some fractures display hydraulic/void apertures ≤ 5 mm, which are related to karstification that mainly developed at the intersection between fracture planes and the associated oblique tectonic stylolites (in blue in Fig. 4C and D).

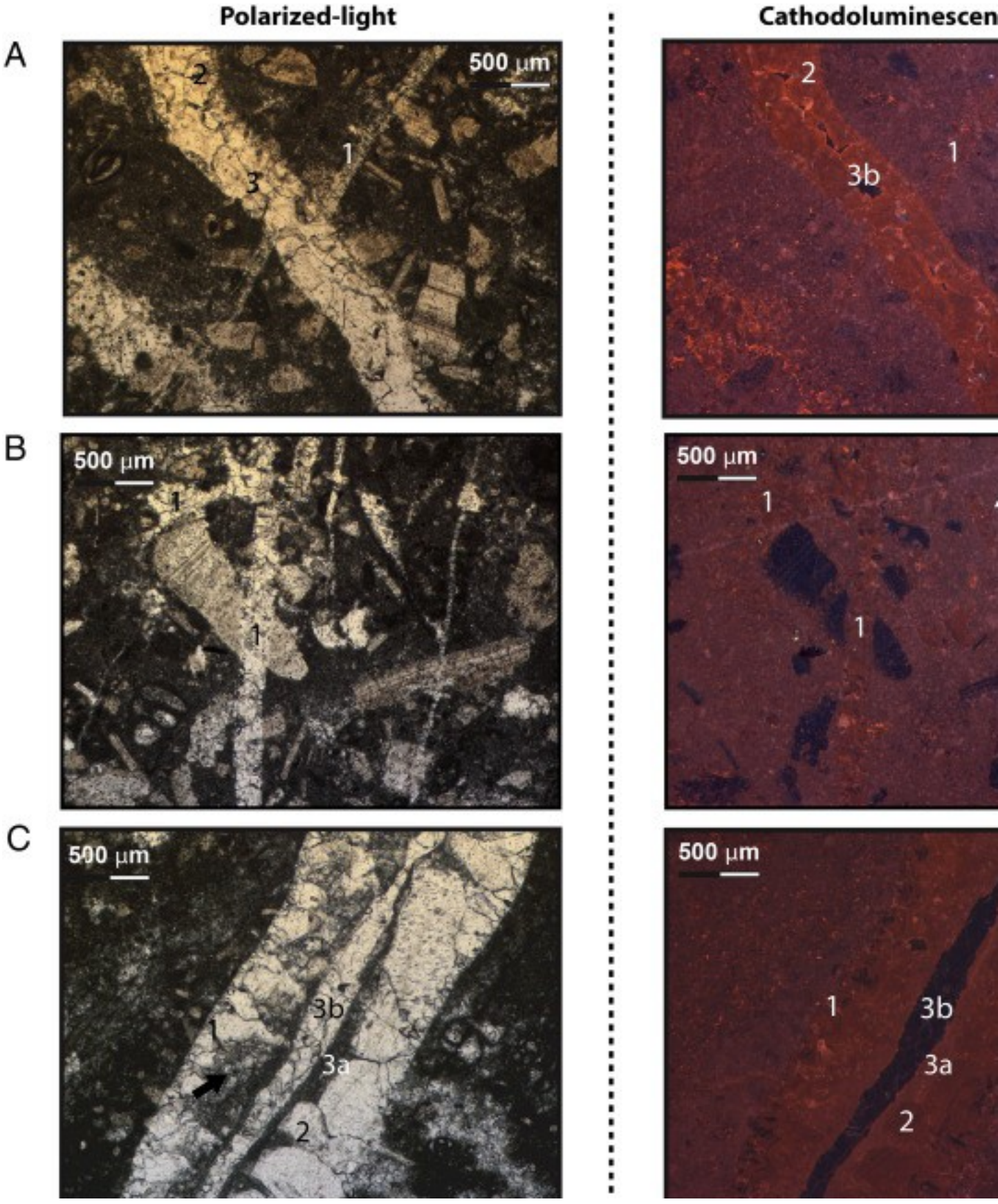
Polarized-light
Cathodoluminescen
A
B
C
500 μm
2
1
3
3b
3a

1. Download high-res image (4MB)
2. Download full-size image

Fig. 5. Microphotographs of the fractures in thin sections. (Left part) images acquired in Polarized light. (right part) images in acquired cathodoluminescence; A: Cross-cutting relationships between reactivated and non-reactivated fractures; B: Non-reactivated fractures filled by one cement phase (1); C: Reactivated fracture with multiple phases of filling cements; D: Reactivated fracture showing wide reactivation cements (2 and 3) and intercrystalline central pores (arrow); E: Karstified fracture exhibiting altered sparite along with large karstic dissolution void (porosity in blue in the left image).

At the microscale, reactivated and non-reactivated fractures differ in terms of width (few-tenths of microns vs. > 1 mm in Fig. 5B–D) and in terms of cementation structure. Cathodoluminescence observations showed that the thinner non-reactivated fractures are filled with one sparitic cement type, which appears as a purple dully-luminescent cement (1 in Fig. 5B). This cement displays the same luminescence as sparite found inside the intergranular space of the rock matrix and intraskeletal spaces of fossils (arrow in Fig. 5B). The reactivated fractures display several phases of cement fringes (at least two phases are always observed). First, on the fracture walls, the same dully-luminescent cement as the one found in the non-reactivated is observed (1 on Fig 5C and D). Then, toward the fracture's center, an orange-to-red luminescent cement is present, generally composed of large sparitic crystals (2 on Fig. 5C and D). The largest sparite crystals (≈ 50 μm) in this cement phase sometimes exhibit a twinned aspect, suggesting shear stress during their precipitation (Burkhard, 1993). This cement phase corresponds to a “synkinematic cement”, sensu Laubach (2003). These two cement phases are often smoothed and partially fractured, forming sheared and crushed calcite zones inside the fracture filling (arrow in Fig. 5D). A third highly luminescent micritic fringe associated with dissolution of the previous cement (2 on Fig. 5) is observed in some reactivated fractures (3a in Fig. 5C). This dissolution forms a sinuous karst-conduit shape where the micritic and latter cements take place. A fourth sparitic non-luminescent dark blue cement occurs in the center of the fracture (3b in Fig 5A and C–E), sometimes alternating with banded orange highly luminescent cement. It is likely related to a meteoric diagenetic environment, considering its luminescence and the dissolution phase that predate it (e.g., Muchez et al., 1998, Vandeginste et al., 2012). Finally, a few reactivated fractures contain micron to few-tenths-of-micron-wide pores in the center of the fracture's filling, between sparite crystals or inside gaps of cements (Fig. 5E).

4. Block P-wave velocity measurements analysis

4.1. V_p variations with raypath dip angle and fracture density

The 1298 computed P-wave velocity (V_p) values gathered from the vertical geophysical cross section range from 3626 to 6785 m/s, but exhibit a relatively small standard deviation of 395 m/s. Fig. 6A shows six histograms of V_p versus the number of cemented fractures crosscut/intersected by each raypath. The figure illustrates that (i) the largest variability of $V_p$between 3620 and 6785 m/s is found for raypaths with no intersected fracture; (ii) the average V_p value of each class increases with the number of intersected fractures; and (iii) the higher the number of intersected cemented fractures, the lower is the V_p variance (which is a minimum for raypaths intersecting > 20 fractures). However, V_p variations as a function of the linear cemented fracture density (in fractures/m, calculated for each raypath) indicate that V_p values are still scattered for a given fracture density (approximately 800 m/s, Figs. 6C and A2). In detail, a gap in the V_p values occurs around 6250 m/s, and this gap tends to disappear at high fracture density.

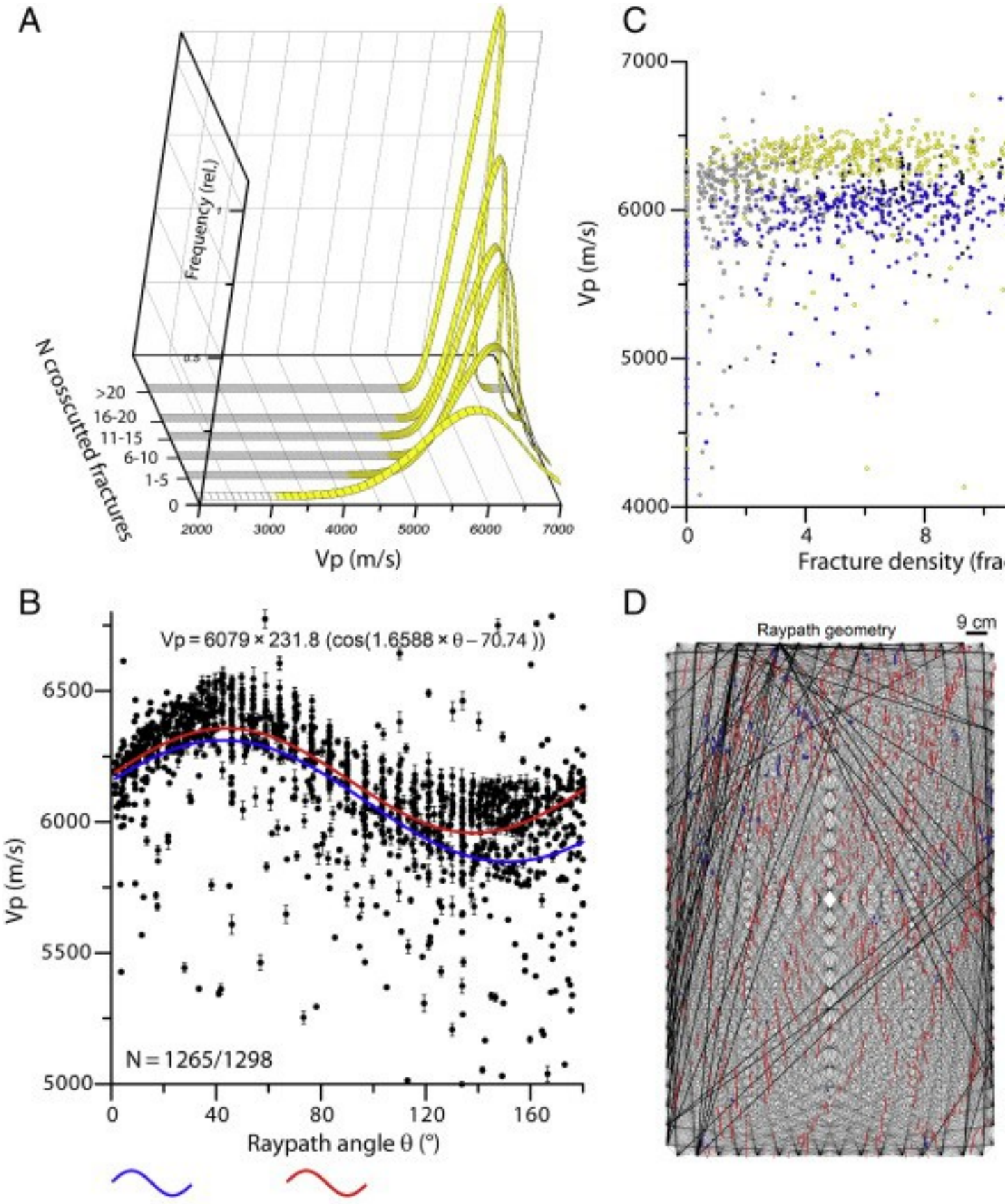
A
Frequency (rel.)
1
0.5
N crosscutted fractures
>20
16-20
11-15
6-10
1-5
0
2000
3000
4000
5000
6000
7000
Vp (m/s)
C
7000
6000
5000
4000
Vp (m/s)
0
4
8
Fracture density (fra
B
Vp = 6079 × 231.8 (cos(1.6588 × θ – 70.74))
6500
6000
5500
5000
Vp (m/s)
N = 1265/1298
0
40
80
120
160
Raypath angle θ (°)
D
Raypath geometry
9 cm

1. Download high-res image (2MB)
2. Download full-size image

Fig. 6. A: Fitted histogram of the P-wave velocity for different amount of crosscutted cemented fractures; B: Plot of the V_p vs. raypath dip angle (error bars are figured); C: Variations of V_p vs. the linear fracture density, with the colors indicating the raypath dip angle of each V_p value; D: Geometry of the $V_p$measurement raypaths on the block structural map, defining the raypath angle θ. The bold lines are the rays corresponding to V_p < 5600 m/s.

V_p variations as a function of raypath dip angles θ indicate that V_p values are strongly correlated with the dip angle of the raypaths following a sinusoidal relationship (θ = 0° vertical and θ = 90° horizontal, in Fig. 6B and D). Indeed, V_p for ray dip angles around 40° is about 500 m/s higher than V_p values for angles around 140°. However, sparse, weakly-correlated to θ, low V_p values of under 5600 m/s are present. Most of these low values are measured for raypath dip angles ranging between 100 and 160°. We fitted the V_p vs. θ angle relationship using the optimization method based on a trigonometric equation in MATLAB. The blue curve was fitted in Fig. 6B including the entire dataset. The fitting indicates that $V_p$vs. θ angle correlation follows a sinusoidal variation characterized by a phase shift of 35°, a period of 217°, and a significant amplitude of 231 m/s (indicating an average maximum Vp variation of 461 m/s). Moreover, after removing the low, poorly correlated, V_p values (red curve in Fig. 6B), the fitting parameters slightly change: the amplitude decreases to 199 m/s, corresponding to a 15% decrease in the V_p angular anisotropy, the phase slightly changes to 45°, and the period decreases to 188°.

In contrast, in the horizontal ultrasonic cross section performed 15 cm below the block's upper surface (along horizontal XY plane, Fig. 2), the 528 V_p values show no clear angular (azimuthal in this case) anisotropy (Fig. 7), and the V_p values fall mostly around 6000 m/s. However, we also find here very low V_p values of < 5000 m/s, especially in the direction perpendicular to the N065, i.e., the average fractures direction in the block (Figs. 3E and 4C).We found no low values parallel to this direction.

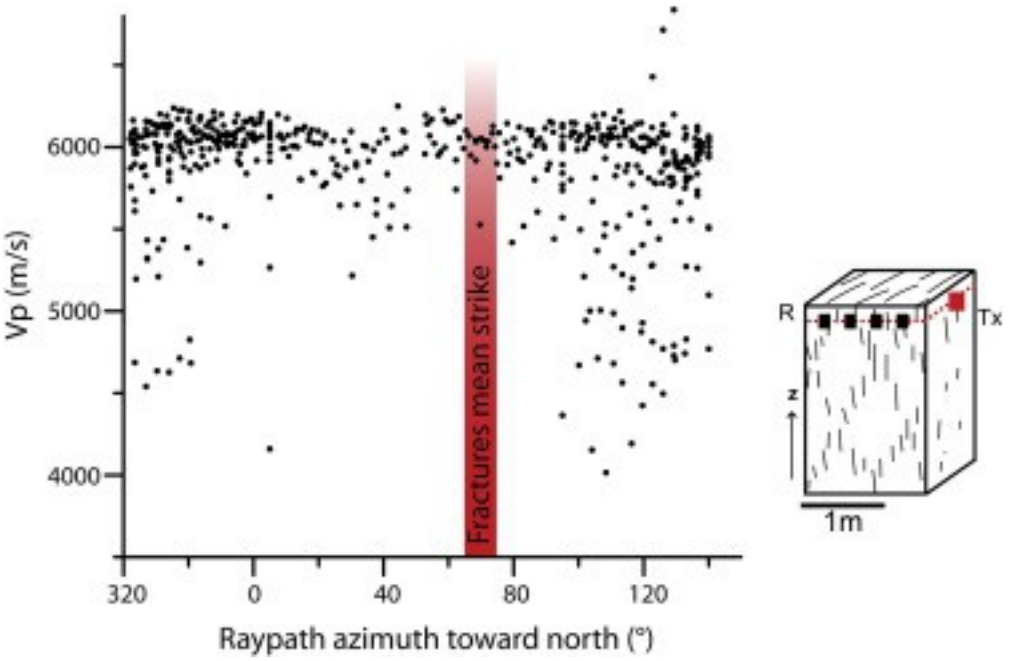

1. Download high-res image (172KB)
2. Download full-size image

Fig. 7. V_p vs. raypath azimuth, from the horizontal geophysical cross-section showing non-anisotropic variations.

Examining the ray dip angle θ attribute shown in the V_p vs. fracture density plot (colors in Fig. 6C), the point cloud appears to be now rather well discriminated, exhibiting two main velocity point sets. The 20 to 80° class (yellow points on Fig. 6C) displays V_p values 500 to 1000 m/s higher than the 95 to 160° class (blue points on Fig. 6C), which are both widespread in terms of fracture density values. These two point sets are separated by the gap in V_p values discussed before. Interestingly, the subvertical raypaths (θ between 160 and 20°, gray points in Fig. 6C), which obviously intersect a limited number of fractures, exhibit no velocity values gap around 6250 m/s and are scattered over a wide range of velocities. The sub-horizontal raypaths (black points on Fig. 6C) correspond to a few points occurring at a wide range of fracture densities (from 1 to > 12 fractures/m) and are centered around 6200 m/s.

4.2. Impact of the fractures diagenetic evolution on P-wave velocity and anisotropy

In the following section, we interpret the velocity variations observed in the light of the fracture pattern present on the block's vertical face (ZY plane in Fig. 2, Fig. 4B). Considering that fractures show an elongated elliptic shape (strike length > height, Fig. 4C–D), along with little strike variation (around N070 on average, Fig. 3E) we can

reasonably assume that the fractures visible on the block face are surely present at 15 cm below its surface (where the ultrasonic cross section was performed).

In the vertical geophysical cross section, we measured an overall increase of V_p with fracture density (Fig. 6A). This seems a counterintuitive result, because fractures are known to reduce the global mechanical moduli of rocks, thus to reduce V_p (Hudson, 1981, King et al., 1986, Lubbe and Worthington, 2006, Moos and Zoback, 1983, Pyrak-Nolte et al., 1990b, Watanabe and Sassa, 1995,). This highlights the strong impact of the fracture's filling material on the seismic wave propagation. Indeed, this result is in good accordance with Ass'ad et al. (1993), who showed that no first arrival-time delay occurs for waves travellingthrough synthetic fractures filled with a high-mechanical-moduli material. Here, the mainly sparitic calcite filling of fractures increases their elastic stiffness, maybe to levels above the stiffness of the surrounding intact micritic rock. For instance, Vanorio and Mavko (2011)underlined that for non-porous material, pure micrite exhibits lower stiffness and ultrasonic velocity than pure sparite. Hence, when the fracture density is high (Figs. 6A, C and A1), the proportion of sparite compared to micrite crossed by a ray is increased, resulting in a masking of potential lower velocity in the intact (mainly micritic) host rock, or yielded by other features such as karstified fractures.

We found from the vertical ultrasonic cross section a magnitude of V_p anisotropy as high as 8% on average and 16% at maximum (Fig. 6B) between the 40° and 140° raypath dip angles. These angles of 40° and 140° correspond (Figs. 3A and 4B–D) to the dip angles of the non-reactivated and reactivated fractures clusters, respectively. This means that P-waves travelling along raypaths following these two dip angles have respectively intersected preferentially non-reactivated or reactivated fractures. Moreover, the intact sedimentary facies of the block is characterized by a micrite-rich inner platform facies, i.e., it corresponds to a very low energy depositional environment that displays little heterogeneity, no sedimentary structures, or porosity variations able to influence directional V_p variation. Such a rock type could very unlikely be a source of perturbation of the geophysical anisotropy measured here. Consequently, we can assume that the measured anisotropy is very likely caused by the reactivation of one of the two fracture clusters (dipping 55°W, Figs. 3A, C and 4B). Our measurements thus underline the acoustic signature of the fracture reactivation at the meter/sub-seismic scale, which is characterized by a V_p decrease from 500 to 1000 m/s. Such a velocity decrease, associated with reactivated fractures, implies that they are characterized by higher compliance than the non-reactivated ones (Lubbe and Worthington, 2006, Pyrak-Nolte et al., 1990a), even if they are both cemented.

This idea is clearly reinforced by (i) the intermediate velocities (around 6200 m/s) found in the horizontal rays of the vertical geophysical cross section (black points in Fig. 6C), and by (ii) the more isotropic velocities found in the horizontal cross section (Fig. 7). In both cases, this is because all these rays in the horizontal plane have an equal probability to intersect fractures from the reactivated or non-reactivated clusters, thus averaging the V_p signature coming from these two types of fractures. Two causes may explain the slightly lower velocity found in the horizontal geophysical cross section (median V_p = 6007 m/s) compared to the V_p from the horizontal rays of the vertical cross section (around 6200 m/s). First, because one side of the block was inaccessible for the horizontal cross section (Fig. 4A), fewer rays were subparallel to the fractures and karsts. Therefore in these measurements, numerous rays crosscut more perpendicularly the fractures, decreasing V_p more than if they have crosscut fractures with a high incident angle (e.g., Pyrak-Nolte et al., 1990b, Vilhelm et al., 2013). Second, the top face of the block, close to the location of the horizontal geophysical cross section (Fig. 2A), was the quarry ground floor before the block was extracted. This block face may thus have been more affected by current meteoric alteration/karstification (Fig. 4A and C).

More precisely, in terms of V_p signature of fracture reactivation, the two point sets (yellow and blue) highlighted in Fig. 6C, correspond to raypath dip angles in the range of the two fracture clusters' dip. Indeed, in Fig. 6C these two point sets are separated by the gap of $V_p$values around 6250 m/s. This gap seems to be related to the contrast existing in fracture properties, as suggested by its absence for subvertical rays (cutting few to no fractures, cf. gray points in Fig. 6C) and by the 6200 m/s median value of sub-horizontal rays that cut equal numbers of the two fracture types at high fracture density (black points in Fig. 6C). We can consider that this lack of values around 6200 m/s may accounts for the smallest possible V_p difference between the non-reactivated and reactivated fracture signatures.

Finally, the lowest values of V_p (< 5600 m/s) observed in the vertical geophysical cross section correspond to raypaths passing across zones where numerous karstified fractures occur, especially in the upper left corner of the block (Fig. 4B and D, and bold lines in Fig. 6D). Karst or large voids are known to decrease P-waves velocities in carbonate rock (e.g.; Hall et al., 2001, Gu et al., 2006, Samyn et al., 2014). Moreover, in the horizontal cross section (Fig. 7) the same low V_p values (< 6000 m/s) are observed, especially for rays mostly perpendicular to the fracture's strike, i.e., rays that have more probability to crosscut fractures and thus karstified fractures. Therefore our measurements highlight the acoustic signature of fracture karstification, which causes

this dramatic decrease in V_p compared to cemented or even tectonic-reactivated fractures, exhibiting V_p values between 3600 and 5600 m/s. This low V_p signature of karst also likely explains the high variance and the low $V_p$values observed for raypaths intersecting few-to-zero cemented fractures (Figs. 6D and A2). These low values may be more the result of the combination of the intact sedimentary facies with V_p signatures of karstified fractures.

According to the comparison of the two fits (blue and red curves in Fig. 6B), the fracture karstification would be responsible for only 15% of the total anisotropy; hence, the main part of the V_p anisotropy being caused by the reactivated fractures in shear (Fig. 9B and C, “reactivation” step). Note that most of the karst signature V_p values are observed for raypaths dip angles between 100 and 160° (Fig. 6B), i.e., in the reactivated fracture cluster's dip angles range, suggesting that tectonic reactivated fractures, even when calcite filled, are more sensitive to the karstification process.

4.3. Contribution of first arrival-time tomography on the 2D meter scale imaging of the fracture reactivation and karstification

A tomographic reconstruction of V_p variations was performed from the vertical geophysical cross-section measurements, located 15 cm below the block's vertical face (cf. part 2 and Fig. A1). The velocity model (Fig. 8) is composed of 400 V_p cells and shows velocities between 4928 and 6485 m/s, which is a slightly narrower range than for the velocities computed from each raypath.

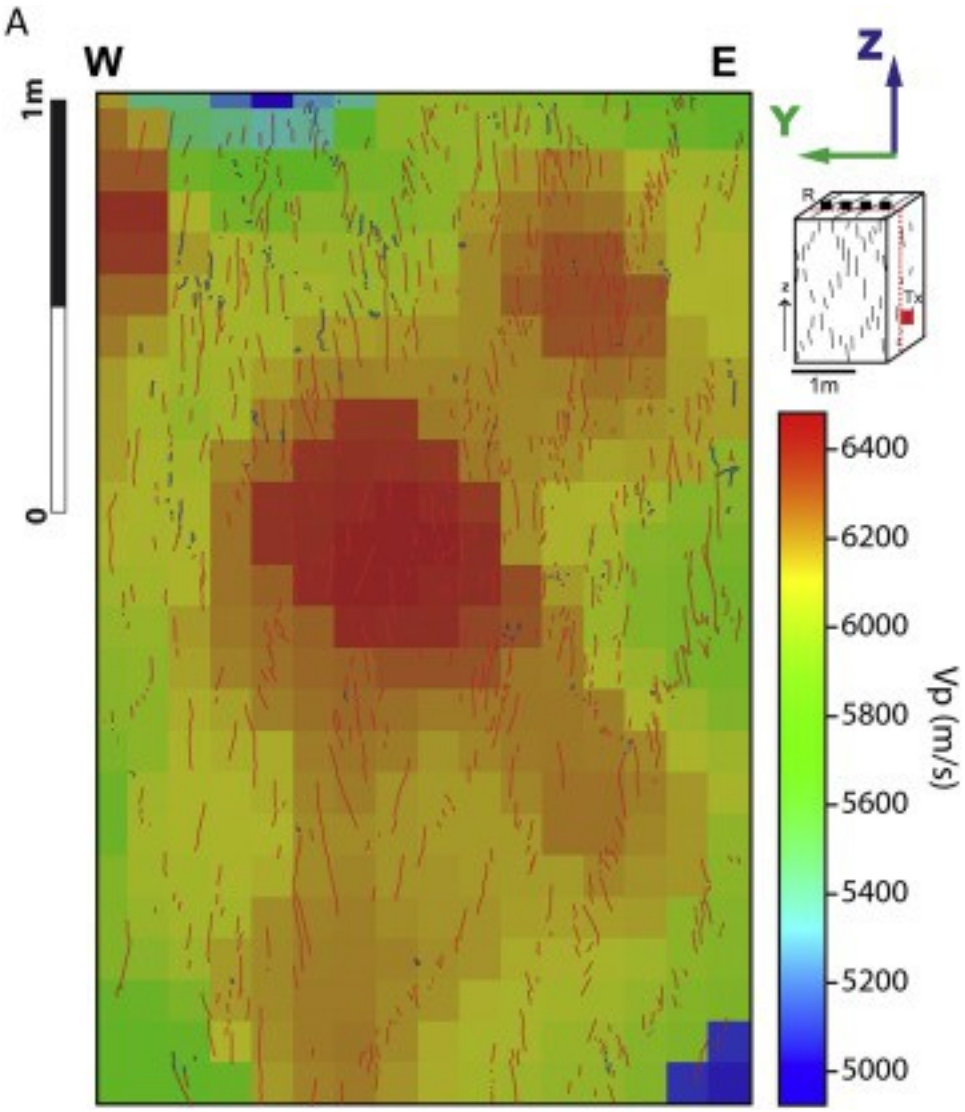

1. Download high-res image (406KB)
2. Download full-size image

Fig. 8. A: Two-dimensional V_p tomography image from the vertical cross-section measurements (RMS = 0.029), with structural features mapped on.

On this model we first observe, oblique bands (decimeter-wide) of homogeneous velocity:

- A central band of high velocity, around 6400 m/s (orange to red in Fig. 8). The dip of this band to the east corresponds to the non-reactivated fracture clusters' dip direction.
-

Slightly lower velocity bands characterized by V_p around 6000 m/s (in green to yellow in Fig. 8), dipping to the west and corresponding to the reactivated fracture clusters' dip direction.

These oblique bands display similar velocities to the average velocities for raypaths passing through the respective non-reactivitated and reactivated fracture clusters (Fig. 8). They are also compatible with the dip and the width of the fracture clusters. Moreover, in the $V_p$model, the lower V_p bands dipping to the west crosscut and overlap the central high velocity band (e.g., in the upper left and lower right parts of the model in Fig. 8).This is compatible with the fractures' relative chronology, i.e., the fact that reactivated fractures crosscut and offset non-reactivated ones. Thus this tomography reconstruction seems to accurately capture the pattern and anisotropy of the V_p variations observed for the individual raypaths velocities and may provide a crude image of the fracture clusters.

Second, we observe lower velocity zones, < 6000 m/s, located for instance on the top left part of the block (in blue in Fig. 8), where numerous karstified fractures occur. However, these low velocities are not present in all karstified zones that are visible on the block's face. This is likely due to the fact that some voids inside the karstified fractures do not reach the 15 cm “depth” below the block face (where V_p measurements were performed), as the cements infilling in the karstified fractures are only partially dissolved and remain mainly continuous (Fig. 4, Fig. 5E).

Moreover these low V_p zones are of greater dimension than individual karstified fractures, which could indicate that what we image here are more likely whole karstified zones, rather than individual voids in fracture internal spaces. Indeed, Gu et al. (2006) performed $V_p$tomography at hectometer scale, using similar measurement geometry and the SIRT algorithm, but using a10 KHz source peak frequency. They pointed out low velocity zones (< 5000 m/s) that corresponded to open fractured zones or karstic voids of tenths of meters scale, i.e., of a size much larger than the wavelength of the signal used. This suggests that in our case, void dimensions in individual karstified fractures are too small compared to the tomography resolution, using only first arrival-time inversion. Indeed, following Williamson (1991), a signal wavelength λ of about 9° cm considered here gives us a maximum resolution between 10 and 50 cm (depending on the raypath lengths). Hence, velocity contrasts yielded by individual reactivated fractures are *a fortiori* also too small to be precisely resolved with this inversion technique, but might be resolved using Full Waveform Inversion (e.g., Wu and Toksoz, 1987). Therefore, in our case, with this source frequency, anisotropy may partially (at least for the longest raypaths > 2 m measurements) result from the effect of

the whole reactivated fracture cluster structure/bodies, i.e., the addition of the effect of numerous reactivated fractures, characterized by higher compliance.

5. Discussions on the processes inducing anisotropy and their timing

Several previous works (e.g., Crampin and Lovell, 1991, Prioul et al., 2004, Sayers and Kachanov, 1995) performed in the laboratory and in reservoir conditions highlighted that ultrasonic velocity anisotropy is partly (even entirely) due to the three-dimensional stress state applied to a rockmass or to individual fractures (Pyrak-Nolte, 1996). This stress opens existing cracks or results in newly formed micro-cracks (< 0.1 mm width) aligned parallel to the principal stress direction (Sayers and Vanmunster, 1991). However, in our study, the stress effect cannot be considered as the source of the current geophysical anisotropy, since the studied block is now unconfined at the ground surface. We found no such effects in our study. Indeed, un-confinement stress effects on the block boundaries were not pointed-out because no velocity variations were found for rays parallel to the block faces. Besides, such effects are unlikely to lead to the oblique anisotropy we evidenced in our data. Therefore we can assume that the V_p anisotropy we observe is not related to the current stress state. We suggest that this observation is explained by the high cementation of the block's fractures and host rock matrix (porosity < 1.5%) that maintained the block's mechanical cohesion throughout its exhumation history (Fig. 9A). This is in accordance with Olson et al. (2009), who have shown that partial fracture cementation, which partly depends on fracture size (Laubach, 2003), or pervasive matrix cementation, can stiffen the host rock, even without completely sealing the fractures. Besides, it has been demonstrated that micro-cracks in reservoir condition and under sufficient temperature can be filled very readily (e.g., Anders et al., 2014, Lander and Laubach, 2015) and become insensitive to stress variations. Indeed, except for the karstified fractures, we did not find non-continuous cements in fractures or bridge cements in the fractures on thin sections.

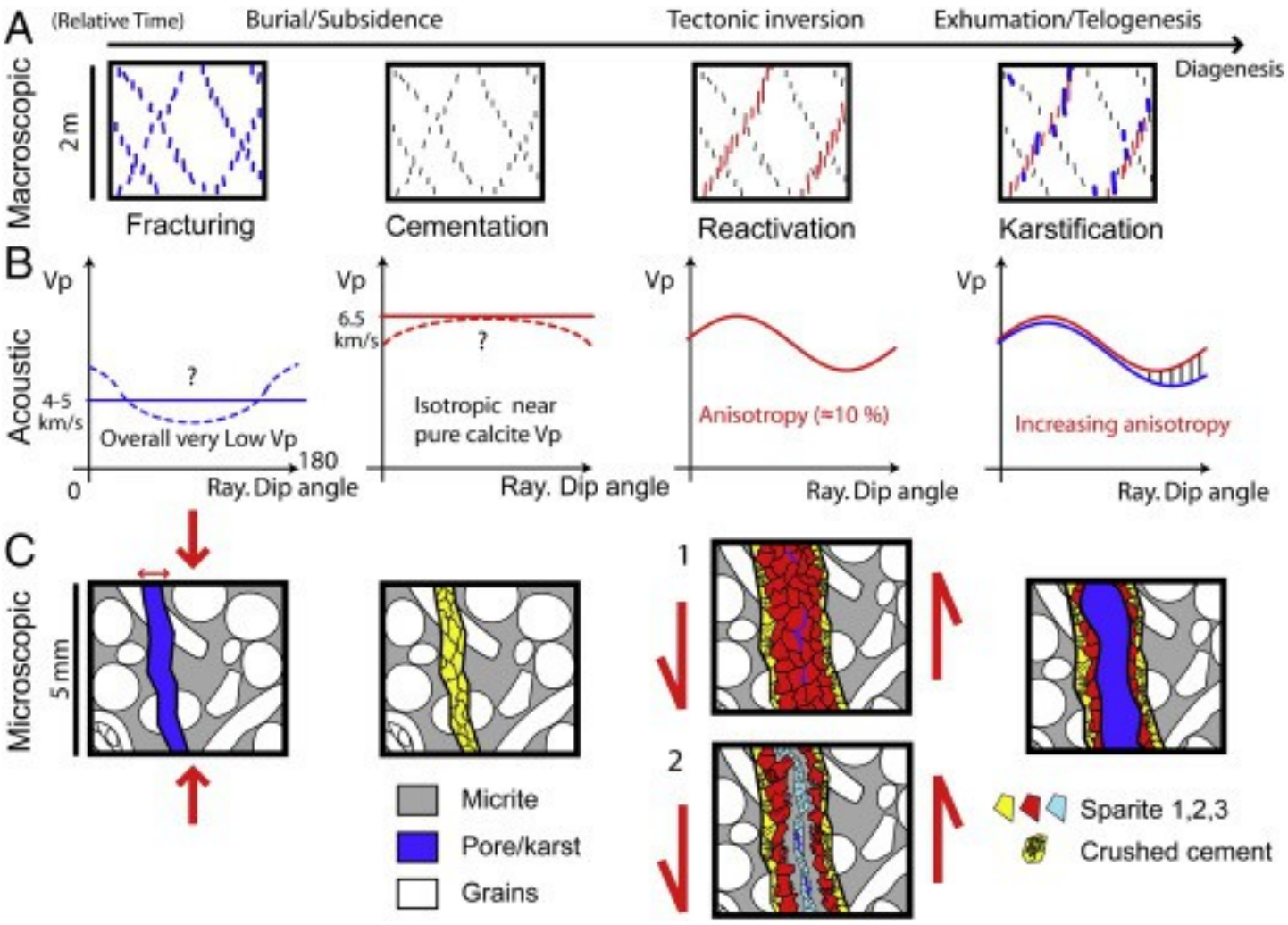

1. Download high-res image (589KB)
2. Download full-size image

Fig. 9. Conceptual diagram showing the evolution of the acoustic signature of fractured carbonate during the structural diagenesis of a sedimentary basin.

Here we show that the variation of the properties of the fracture filling materials likely controls the V_p anisotropy (Fig. 6B). As a matter of fact, reactivated fractures contain different and heterogeneous filling material compositions (layers of cement with different calcite crystal sizes, brecciated zones, and intercrystalline pores; Fig. 5) compared to the non-reactivated ones (cf. 3.2 and Fig. 9C, “cementation” and “reactivation” steps). In first order, the very flat intercrystalline pores found in some of the reactivated fractures are of a pore type that favors a strong decrease of V_p, more than any other pore types (Baechle et al., 2008, Fournier et al., 2011). Then, as indicated by several laboratory studies performed on samples (Ass'Ad et al., 1993, Boadu and Long, 1996, Leucci and De Giorgi, 2006, Matonti et al., 2015), the

fracture infilling material can modulate (even cancel) the way fractures impact wave propagation and velocities. In addition, brecciated sparite layers, formed during the fracture strike-slip reactivation, constitute a softer material than intact sparite. Fortin et al. (2007) and Acosta-Colon et al. (2009) noted the effect of grain crushing, grain size reduction, and layering of infilling material on the decrease of the P-wave velocity. Here, the multiple cement layer interfaces in the reactivated fractures may also lower the overall fracture stiffness compared to those filled with a single blocky sparite cement phase, tightly sealing the non-reactivated fracture (Fig. 9C "reactivation" step). Such a difference, in terms of reactivated fracture infilling material, may make it more sensitive to meteoric karstification. This fact very likely explains why we found more low V_p karst signatures for the angle range corresponding to the reactivated clusters (Figs. 6B and 7), thus amplifying the V_p anisotropy (Fig. 9 "karstification step"). Finally, reactivated fractures are also longer than the non-reactivated ones, which may confer them higher compliance (as observed by Guglielmi et al., 2008, Zangerl et al., 2008, Worthington and Lubbe, 2007) compared to non-reactivated ones by increasing the probability of fracture mechanical connectivity (Marrett et al., 2007). This could also be a factor in the velocity decrease found in the reactivated fracture cluster direction.
Consequently, a significant result of this study is to highlight the importance of the evolution of the natural fracture infilling produced by the tectonic reactivation, which here is the key phenomenon to explain velocity anisotropy. We identified mechanisms that induce anisotropy, and mechanisms that may eventually amplify or reduce it.

The initial fracturing, by producing open fractures with > 1 to few mm apertures, tends to reduce the overall V_p to velocity comparable to the current karstified fracture signature. Because all fractures were initially open (Fig. 9 "fracturing" step), and because fracturing implies that the host rock matrix was already stiffened/tight, we can assume that this process yielded a low V_p with nearly isotropic signature (< 6000 m/s), as long as the fractures remained open (Fig. 9B–C "fracturing" step). This fracturing process took place during the basin subsidence, after the lithification, while the Cenomanian rocks were buried, as indicated by the "conjugate clusters" fracture pattern and by the inferred vertical σ_1 (Figs. 3A, B and 4B). The non-preferred orientation of crystal growth of the first phase of cement filling fractures (1 in Fig. 5), i.e., the occurrence of blocky, few elongated sparite, instead of fibrous or stretched calcite crystals, may indicate that the fracture cementation did not take place during the fracturing process (Petit et al., 1999, Bons et al., 2012, Bons and Montenari, 2005). This observation means that fractures remained open during the period after the fractures

formed and before the cementation phase, suggesting that the low isotropic $V_p$signature has been transient but existed during a sizeable time (Fig. 9B).

Next, the complete cementation of all the fractures during burial, between the Turonian and the basin tectonic inversion at the end of Cretaceous, induced an increase of velocity to a value possibly even higher than the initial facies velocity (Fig. 9 “cementation” step). This cementation of all fractures (in both *en-échelon* clusters) provided isotropic high V_p to the rocks, near the pure calcite V_p value, as underlined by the high V_p signature of cemented non-reactivated fractures (Fig. 6, Fig. 9B). Note that the similar luminescences observed between the first fracture cement phase and the intergranular sparite cements (1 in Fig. 5) suggest that fracture cementation was initiated relatively early during the burial of these rocks.

Then, in our study, the fracture reactivation caused dilatant shear, and allowed for multiple cementation/dissolution phases and crushing of cement asperities. It is the dominant mechanism that induces anisotropy (Fig. 9, “reactivation” step). It is associated with the formation of oblique stylolites along with highly twinned calcite. These features imply respectively a relatively high burial depth/confinement and a tectonic shear stress during precipitation of this cement (1 in Fig. 9C). This process seems to have occurred at least two times, in the fractures that show all the cements and brecciating phases (Fig. 9C “2”). Therefore, the fracture reactivation likely occurred at the onset of the sedimentary basintectonic inversion when these rocks were still sufficiently buried. The fractures newly re-opened by reactivation were likely filled with calcite-saturated fluids presumably enriched by the tectonic stylolite/pressure-solution mechanism, concomitant with the tectonic inversion (Carrioschaffhauser and Gaviglio, 1990, Richard, 2014).

The fact that this burial imprint of fracture reactivation on V_p is still observed in this currently exhumed block indicates that burial conditions are required to generate strong anisotropies in sedimentary rocks, but are not mandatory to maintain it. This suggests that geophysical anisotropy can originate even from sealed fracture networks. It is also a good argument to reasonably argue that this phenomenon may be used to monitor/identify fracture-sealing events at depth. Finally, since these rocks have been sufficiently exhumed to reach the water table zone, the karstification process induced by meteoric dissolution created significant voids inside the fractures (Fig. 9C), preferentially in the reactivated ones. The karstification process acts only as a second-order amplification phenomenon of the $V_p$anisotropy magnitude (Fig. 9, “karstification” step).

6. Conclusions

In this study, by combining multidisciplinary methods, we explored the links existing between fracture properties and geophysical signature of carbonates at the sub-seismic or meter scale, revealing the importance of the microstructural properties of fractures. We found P-wave velocity anisotropy of 8 to 16% related to the fracture reactivation in shear of pre-existing burial mode 1 fractures. This anisotropy was amplified later by the karstificationprocess. These results particularly emphasize that the seismic signature of fractured carbonates is closely related to the fractures' diagenetic and tectonic evolution. We showed that (i) mode 1 fracture opening seems to non-trivially enhance the fracture sealing, thus the isotropy of carbonate rocks, whereas (ii) fracture reactivation in shear mode (mode 2 or 3) lead contrarily to geophysical anisotropy by modifying the nature and the complexity of fracture infilling composed of softer materials. (iii) This underlines that even a sealed and non-permeable fracture network can generate geophysical anisotropy in carbonates.
An interesting contribution of this study is to point out that the occurrence of V_p anisotropy where only cemented fractures are present may be a factor to consider in interpreting geophysical data, as it is not correlated to the current permeability tensor. For instance, it may be considered in interpretations of cross-hole tomography, horizontal well sonic data, or directional sonic wells log which use comparable wave sources frequency than the one used this work. This work might also provide an interesting framework in interpreting of seismic VSP or AVOA data, if we anticipate that these results can (at least partially) extend to higher scales; this may be valid considering that fractures networks can be of far greater dimensions.
One promising perspective of this work is to suggest that even relatively far from faults (i.e., outside the fault-zone sensu stricto, relative to their throw magnitude), fractured rocks can be subject to the effects of tectonic shear over wide areas, sufficiently to be caught/recorded by geophysical methods and implying that very little (millimetric) slip in fracture can generate geophysical anisotropy at the meter scale. Future works should be then dedicated to better characterize the evolution of fractured rocks' geophysical signature in volumes located closer to and inside the faults' macroscopic deformation zones.

Acknowledgments

The authors would like to express their gratitude to ParadigmGeo and ASGA for providing Gocad software and research plugins. This research is supported by OSU-Pytheas Instituteof which CEREGE laboratory is a part. The authors want to thank particularly Marilyn Saarni from Lawrence Berkeley National Laboratory, for valuable

language and grammar corrections that greatly improved this manuscript. We want also to thank CEREGE St-Charles site present and former staff, especially Lisa Texier, Arnaud Gallois, Arezki Chabani, Melody Lefevre, Dawin Baden and Romain Lacube for their help during acoustic on field measurements. We also thank Pr. Marc Floquet for interesting and useful discussion on diagenesis timing. And finally, we would like to say thank you to Philippe Joly for allowing us to access Orves quarry for our study.

Appendix A.

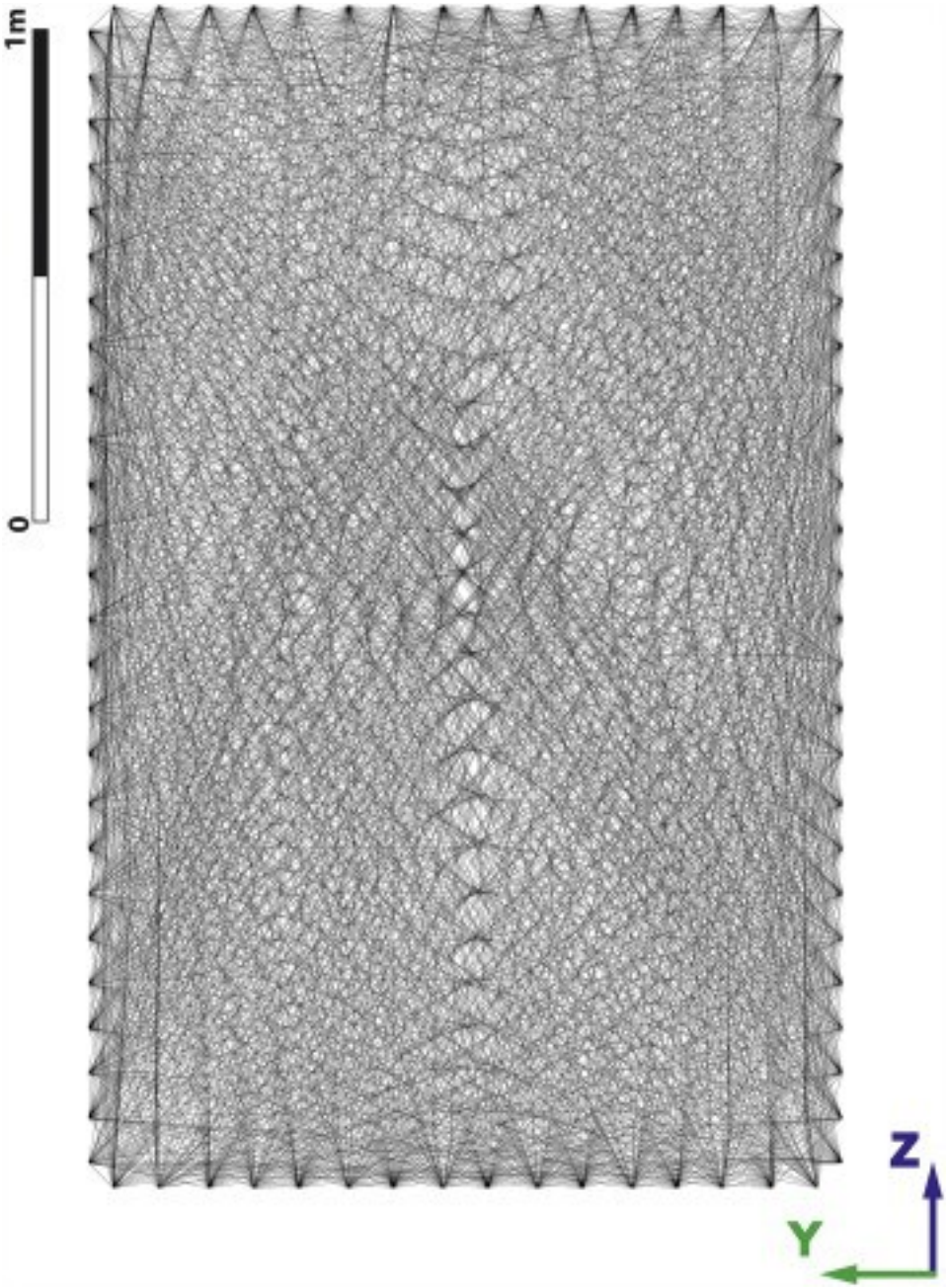

1. Download high-res image (2MB)

2. Download full-size image

Fig. A1. Curvilinear raypath geometry computed from tomographic inversion of the vertical geophysical cross-section.

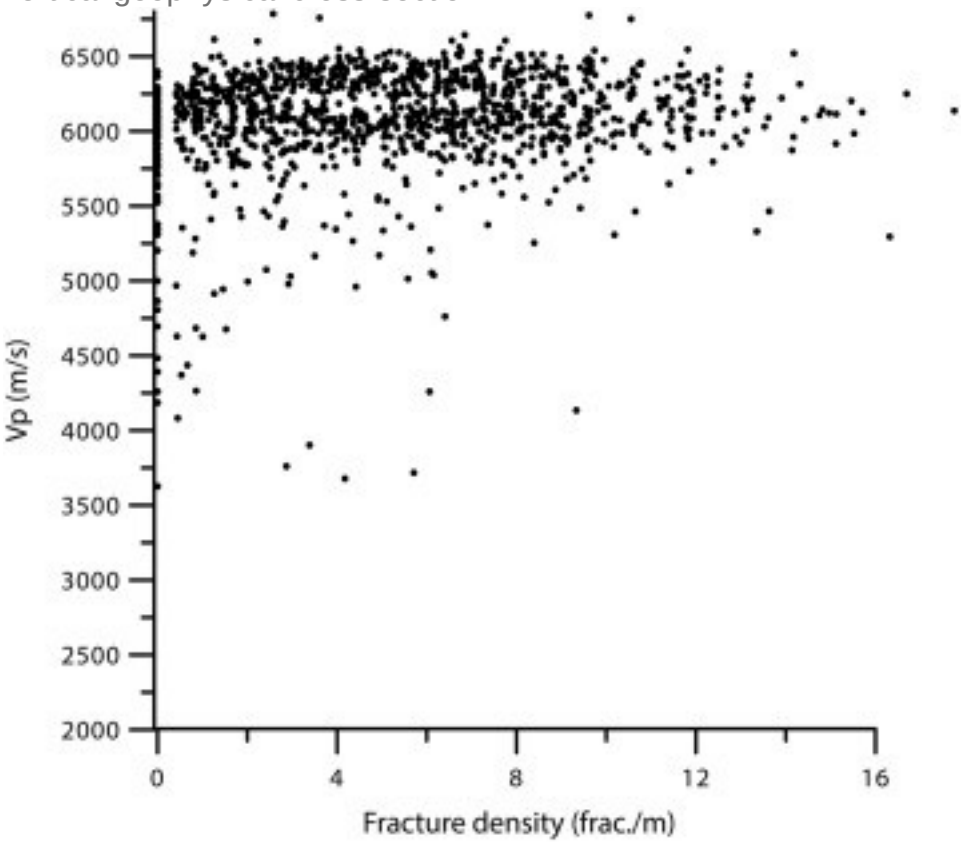

1. Download high-res image (203KB)
2. Download full-size image

Fig. A2. V_p variation vs. fracture linear density plot (all points).

References

Acosta-Colon et al., 2009

A.A. Acosta-Colon, M.K. Olander, L.J. Pyrak-Nolte**Seismic wave propagation across partially in-filled fractures**

Proceedings of the Project Review, 1, Geo-Mathematical Imaging Group (2009), p. 11

View Record in Scopus

Aguilera, 1998

R. Aguilera**Geologic aspects of naturally fractured reservoirs**

Lead. Edge, 17 (1998), pp. 1667-1670

CrossRefView Record in Scopus

Ali and Worthington, 2011

M.Y. Ali, M.H. Worthington**Seismic modelling of a fractured carbonate reservoir in Abu Dhabi, United Arab Emirates**
Geoarabia, 16 (2011), p. 17
CrossRefView Record in Scopus

Anders et al., 2014

M.H. Anders, S.E. Laubach, C.H. Scholz**Microfractures: a review**
J. Struct. Geol., 69 (Part B) (2014), pp. 377-394
ArticleDownload PDFView Record in Scopus

Anderson, 1951

E.M. Anderson**The Dynamics of Faulting and Dyke Formation With Applications to Britain**
Hafner Pub. Co. (1951)

Ass'Ad et al., 1993

J.M. Ass'Ad, R.H. Tatham, J.A. McDonald, T.M. Kusky, J. Jech**A physical model study of scattering of waves by aligned cracks: comparison between experiment and theory**
Geophys. Prospect., 41 (1993), pp. 323-339
CrossRefView Record in Scopus

Baechle et al., 2008

G.T. Baechle, A. Colpaert, G.P. Eberli, R.J. Weger**Effects of microporosity on sonic velocity in carbonate rocks**
Lead. Edge, 27 (2008), pp. 1012-1018
CrossRefView Record in Scopus

Bestani et al., 2016

L. Bestani, N. Espurt, J. Lamarche, O. Bellier, F. Hollender**Reconstruction of the provence chain evolution, southeastern France**
Tectonics, 35 (2016), pp. 1506-1525
CrossRefView Record in Scopus

Billi et al., 2003

A. Billi, F. Salvini, F. Storti**The damage zone-fault core transition in carbonate rocks: implications for fault growth, structure and permeability**
J. Struct. Geol., 25 (2003), pp. 1779-1794
ArticleDownload PDFView Record in Scopus

Boadu and Long, 1996

F.K. Boadu, L.T. Long**Effects of fractures on seismic-wave velocity and attenuation**
Geophys. J. Int., 127 (1996), pp. 86-110
CrossRefView Record in Scopus

Bons and Montenari, 2005

P.D. Bons, M. Montenari**The formation of antitaxial calcite veins with well-developed fibres, Oppaminda Creek, South Australia**

J. Struct. Geol., 27 (2005), pp. 231-248
ArticleDownload PDFView Record in Scopus

Bons et al., 2012

P.D. Bons, M.A. Elburg, E. Gomez-Rivas**A review of the formation of tectonic veins and their microstructures**
J. Struct. Geol., 43 (2012), pp. 33-62
ArticleDownload PDFView Record in Scopus

Burkhard, 1993

M. Burkhard**Calcite twins, their geometry, appearance and significance as stress-strain markers and indicators of tectonic regime - a review**
J. Struct. Geol., 15 (1993), pp. 351-368
ArticleDownload PDFView Record in Scopus

v i g l i o , 1 9 9 0

E. Carrioschaffhauser, P. Gaviglio**Pressure solution and cementation stimulated by faulting in limestones**
J. Struct. Geol., 12 (1990)
(987 −+)

Crampin and Lovell, 1991

S. Crampin, J.H. Lovell**A decade of shear-wave splitting in the Earth's crust: what does it mean? What use can we make of it? And what should we do next?**
Geophys. J. Int., 107 (1991), pp. 387-407
CrossRefView Record in Scopus

Dines and Lyttle, 1979

K. Dines, J. Lyttle**Computerized geophysical tomography**
Proc. IEEE, 67 (1979)
(–1065)

Fang et al., 2014

X. Fang, M.C. Fehler, Z. Zhu, Y. Zheng, D.R. Burns**Reservoir fracture characterization from seismic scattered waves**
Geophys. J. Int., 196 (2014), pp. 481-492
CrossRef

Floquet and Hen

M. Floquet, J. Hennuy**Evolutionary Gravity Flow Deposits in the Middle Turonian—Early Coniacian Southern Provence Basin (Se France): Origins and Depositional Processes, Submarine Mass Movements and Their Consequences**
Springer Netherlands (2003), pp. 417-424

CrossRefView Record in Scopus

Floquet et al., 20

M. Floquet, P. Léonide, L. Villier, A.-P. Ackouala, A. Bléne**Expressions biosédimentaire, diagénétique, géochimique et tectonique de l'évènement anoxique cénomano-turonien (OAE 2) par les plate-formes carbonatées sud-provencales**
4ème Réunion ASF, Paris (2013)

Fortin et al., 200

J. Fortin, Y. Guéguen, A. Schubnel**Effects of pore collapse and grain crushing on ultrasonic velocities and Vp/Vs**
J. Geophys. Res. Solid Earth, 112 (2007)

Fournier et al., 2

F. Fournier, P. Leonide, K. Biscarrat, A. Gallois, J. Borgomano, A. Foubert**Elastic properties of microporous cemented grainstones**
Geophysics, 76 (2011), pp. E211-E226
CrossRefView Record in Scopus

Fournillon, 2012

A. Fournillon**Modélisation géologique 3D et hydrodynamique appliquées aux réservoirs carbonatés karstiques: caractérisation des ressources en eau souterraine de l'Unité du Beausset (Var et Bouches-du-Rhône, SE France)**
Aix-Marseille Université, Marseille (2012), p. 425
View Record in Scopus

Gale et al., 2010

J.F.W. Gale, R.H. Lander, R.M. Reed, S.E. Laubach**Modeling fracture porosity evolution in dolostone**
J. Struct. Geol., 32 (2010), pp. 1201-1211
ArticleDownload PDFView Record in Scopus

Gratier et al., 20

J.P. Gratier, F. Thouvenot, L. Jenatton, A. Tourette, M.L. Doan, F. Renard**Geological control of the partitioning between seismic and aseismic sliding behaviours in active faults: evidence from the Western, Alps, France**
Tectonophysics, 600 (2013), pp. 226-242
ArticleDownload PDFView Record in Scopus

Gu et al., 2006

H. Gu, C. Cai, Y. Wang**Investigation of fractures using seismic computerized crosshole tomography**
J. Environ. Eng. Geophys., 11 (2006), pp. 143-150
CrossRefView Record in Scopus

Guglielmi et al., 2

Y. Guglielmi, F. Cappa, D. Amitrano**High-definition analysis of fluid-induced seismicity related to the mesoscale hydromechanical properties of a fault zone**
Geophys. Res. Lett., 35 (2008)

Hall et al., 2001

S.A. Hall, R.R. Kendall, J.M. Kendall, C. Sondergeld**Analysis of anisotropic velocities in a core sample and AVOA from a fractured vuggy carbonate reservoir**
Anisotropy 2000: Fractures, Converted Waves and Case Studies (2001), pp. 257-269
View Record in Scopus

Hennuy, 2003

J. Hennuy**Sédimentation carbonatée et silicoclastique sous contrôle tectonique, le Bassin Sud-Provençal et sa plate-forme carbonatée du Turonien moyen au Coniacien moyen: évolution séquentielle, diagénétique, paléogéographique**
(2003)
(p. 2 vol., 252, 284 p.)

Hudson, 1981

J.A. Hudson**Wave speeds and attenuation of elastic waves in material containing cracks**
Geophys. J. R. Astron. Soc., 64 (1981), pp. 133-150
CrossRefView Record in Scopus

King et al., 1986

M.S. King, L.R. Myer, J.J. Rezowalli**Experimental studies of elastic-wave propagation in a columnar-jointed rock mass**
Geophys. Prospect., 34 (1986), pp. 1185-1199
CrossRefView Record in Scopus

Lander and Laub

R.H. Lander, S.E. Laubach**Insights into rates of fracture growth and sealing from a model for quartz cementation in fractured sandstones**
Geol. Soc. Am. Bull., 127 (3–4) (2015), pp. 516-538
CrossRefView Record in Scopus

Laubach, 2003

S.E. Laubach**Practical approaches to identifying sealed and open fractures**
AAPG Bull., 87 (2003), pp. 561-579
CrossRefView Record in Scopus

Laubach and Dia

S.E. Laubach, K. Diaz-Tushman**Laurentian palaeostress trajectories and ephemeral fracture permeability, Cambrian Eriboll Formation sandstones west of the Moine Thrust Zone, NW Scotland**
J. Geol. Soc., 166 (2009), pp. 349-362
CrossRefView Record in Scopus

Laubach et al., 2

S.E. Laubach, J.E. Olson, J.F.W. Gale**Are open fractures necessarily aligned with maximum horizontal stress?**
Earth Planet. Sci. Lett., 222 (2004), pp. 191-195
ArticleDownload PDFView Record in Scopus

Laubach et al., 2

S.E. Laubach, P. Eichhubl, C. Hilgers, R.H. Lander**Structural diagenesis**
J. Struct. Geol., 32 (2010), pp. 1866-1872
ArticleDownload PDFView Record in Scopus

Lavenu et al., 20

A.P.C. Lavenu, J. Lamarche, R. Salardon, A. Gallois, L. Marie, B.D.M. Gauthier**Relating background fractures to diagenesis and rock physical properties in a platform-slope transect. Example of the Maiella Mountain (central Italy)**
Mar. Pet. Geol., 51 (2014), pp. 2-19
ArticleDownload PDFView Record in Scopus

Leucci and De G

G. Leucci, L. De Giorgi**Experimental studies on the effects of fracture on the P and S wave velocity propagation in sedimentary rock (“Calcarenite del Salento”)**
Eng. Geol., 84 (2006), pp. 130-142
ArticleDownload PDFView Record in Scopus

Lubbe and Worth

R. Lubbe, M.H. Worthington**A field investigation of fracture compliance**
Geophys. Prospect., 54 (2006), pp. 319-331
CrossRefView Record in Scopus

Marrett et al., 20

R. Marrett, S.E. Laubach, J.E. Olson**Anisotropy and beyond: geologic perspectives on geophysical prospecting for natural fractures**
Lead. Edge, 26 (2007), pp. 1106-1111
CrossRefView Record in Scopus

Matonti, 2015

C. Matonti**Exploration géophysique des processus de fracturation et de réactivation dans les carbonates à l'échelle métrique**
CEREGE—SRS. Aix-Marseille Université (2015), p. 205
View Record in Scopus

Matonti et al., 20

C. Matonti, Y. Guglielmi, S. Viseur, P.O. Bruna, J. Borgomano, C. Dahl, L. Marie**Heterogeneities and diagenetic control on the spatial distribution of carbonate rocks acoustic properties at the outcrop scale**
Tectonophysics, 638 (2015), pp. 94-111
ArticleDownload PDFView Record in Scopus

Mort and Woodc

K. Mort, N.H. Woodcock**Quantifying fault breccia geometry: Dent Fault, NW England**
J. Struct. Geol., 30 (2008), pp. 701-709
ArticleDownload PDFView Record in Scopus

Moos and Zobac

D. Moos, M.D. Zoback**In situ studies of velocity in fractured crystalline rocks**
J. Geophys. Res. Solid Earth (1978–2012), 88 (1983), pp. 2345-2358
CrossRefView Record in Scopus

Muchez et al., 19

P. Muchez, P. Nielsen, M. Sintubin, D. Lagrou**Conditions of meteoric calcite formation along a Variscan fault and their possible relation to climatic evolution during the Jurassic-Cretaceous**
Sedimentology, 45 (1998), pp. 845-854
CrossRefView Record in Scopus

Nelson, 2001

R. Nelson**Geologic Analysis of Naturally Fractured Reservoirs**
Elsevier Science (2001)

Olson et al., 200

J.E. Olson, S.E. Laubach, R.H. Lander**Natural fracture characterization in tight gas sandstones: integrating mechanics and diagenesis**
AAPG Bull., 93 (2009), pp. 1535-1549
CrossRefView Record in Scopus

Petit et al., 1999

J.-P. Petit, C.A.J. Wibberley, G. Ruiz**'Crack–seal', slip: a new fault valve mechanism?**
J. Struct. Geol., 21 (1999), pp. 1199-1207
ArticleDownload PDFView Record in Scopus

Philip, 1998

J. Philip**Sequences and systems tracts of mixed carbonate-siliciclastic platform-basin settings: the cenomanian-turonian stages of provence (southeastern france)**
Mesozoic and Cenozoic Sequence Stratigraphy of European Basins, SEPM (Society for Sedimentary Geology) (1998), pp. 387-395
CrossRef

Prioul and Jocker, 2009

R. Prioul, J. Jocker**Fracture characterization at multiple scales using borehole images, sonic logs, and walkaround vertical seismic profile**
AAPG Bull., 93 (2009), pp. 1503-1516
CrossRefView Record in Scopus

Prioul et al., 2004

R. Prioul, T. Plona, M. Kane, B. Sinha, P. Kaufman, C. Signer**Azimuthal anisotropy using shear dipole sonic: insights from the AIG 10 well, Corinth Rift Laboratory**
Compt. Rendus Geosci., 336 (2004), pp. 477-485
ArticleDownload PDFView Record in Scopus

Pyrak-Nolte, 1996
L.J. Pyrak-Nolte**The seismic response of fractures and the interrelations among fracture properties**
Int. J. Rock Mech. Min. Sci., 33 (1996)
(787–&)

Pyrak-Nolte et al., 1990a
L.J. Pyrak-Nolte, L.R. Myer, N.G.W. Cook**Anisotropy in seismic velocities and amplitudes from multiple parallel fractures**
J. Geophys. Res. Solid Earth, 95 (1990), pp. 11345-11358
CrossRef

Pyrak-Nolte et al., 1990b
L.J. Pyrak-Nolte, L.R. Myer, N.G.W. Cook**Transmission of seismic waves across single natural fractures**
J. Geophys. Res. Solid Earth, 95 (1990), pp. 8617-8638
CrossRefView Record in Scopus

Queen and Rizer, 1990
J.H. Queen, W.D. Rizer**An integrated study of seismic anisotropy and the natural fracture system at the Conoco Borehole Test Facility, Kay County, Oklahoma**
J. Geophys. Res. Solid Earth, 95 (1990), pp. 11255-11273
CrossRef

Rathore et al., 1995
J.S. Rathore, E. Fjaer, R.M. Holt, L. Renlie**P- and S-wave anisotropy of a synthetic sandstone with controlled crack geometryl1**
Geophys. Prospect., 43 (1995), pp. 711-728
CrossRefView Record in Scopus

Richard, 2014
J. Richard**Large-scale mass transfers related to pressure solution creep-faulting interactions in mudstones: driving processes and impact of lithification degree**
Tectonophysics, 612 (2014), pp. 40-55
ArticleDownload PDFView Record in Scopus

Riedel, 1929
W. Riedel**Zur Mechanik Geologischer Brucherscheinungen**
Zentralbl. Miner. Geol. Palaontol. B (1929), pp. 354-368
View Record in Scopus

Rüger and Tsvankin, 1997

A. Rüger, I. Tsvankin**Using AVO for fracture detection: analytic basis and practical solutions**
Lead. Edge, 16 (1997), pp. 1429-1434
CrossRefView Record in Scopus

Samyn et al., 2014
K. Samyn, F. Mathieu, A. Briti, L. Nachbaur, L. Closset**Integrated geophysical approach in assessing karst presence and sinkhole susceptibility along flood-protection dykes of the Loire River, Orléans, France**
Eng. Geol., 183 (2014), pp. 170-184
ArticleDownload PDFView Record in Scopus

Sayers and Kachanov, 1995
C.M. Sayers, M. Kachanov**Microcrack-induced elastic-wave anisotropy of brittle rocks**
J. Geophys. Res. Solid Earth, 100 (1995), pp. 4149-4156
CrossRefView Record in Scopus

Sayers and Vanmunster, 1991
C.M. Sayers, J.G. Vanmunster**Microcrack-induced seismic anisotropy of sedimentary-rocks**
J. Geophys. Res. Solid Earth, 96 (1991), pp. 16529-16533
CrossRef

Sayers et al., 2009
C.M. Sayers, A.D. Taleghani, J. Adachi**The effect of mineralization on the ratio of normal to tangential compliance of fractures**
Geophys. Prospect., 57 (2009), pp. 439-446
CrossRefView Record in Scopus

Schubnel and Guéguen, 2003
A. Schubnel, Y. Guéguen**Dispersion and anisotropy of elastic waves in cracked rocks**
J. Geophys. Res. Solid Earth, 108 (2003)

Vandeginste et al., 2012
V. Vandeginste, R. Swennen, M. Allaeys, R.M. Ellam, K. Osadetz, F. Roure**Challenges of structural diagenesis in foreland fold-and-thrust belts: a case study on paleofluid flow in the Canadian Rocky Mountains West of Calgary**
Mar. Pet. Geol., 35 (2012), pp. 235-251
ArticleDownload PDFView Record in Scopus

Vanorio and Mavko, 2011
T. Vanorio, G. Mavko**Laboratory measurements of the acoustic and transport properties of carbonate rocks and their link with the amount of microcrystalline matrix**
Geophysics, 76 (2011), pp. E105-E115
CrossRefView Record in Scopus

Vetri et al., 2003
L. Vetri, E. Loinger, J. Gaiser, A. Grandi, L. Heloise**3D/4C Emilio: azimuth processing and anisotropy analysis in a fractured carbonate reservoir**

Lead. Edge, 22 (2003), pp. 675-679
CrossRefView Record in Scopus

Vilhelm et al., 2013
J. Vilhelm, V. Rudajev, T. Lokajicek, R. Zivor**Velocity dispersion in fractured rocks in a wide frequency range**
J. Appl. Geophys., 90 (2013), pp. 138-146
ArticleDownload PDFView Record in Scopus

Watanabe and Sassa, 1995
T. Watanabe, K. Sassa**Velocity and amplitude of P-waves transmitted through fractured zones composed of multiple thin low-velocity layers**
Int. J. Rock Mech. Min. Sci. Geomech. Abstr., 32 (1995), pp. 313-324
ArticleDownload PDFView Record in Scopus

Williamson, 1991
P.R. Williamson**A guide to the limits of resolution imposed by scattering in ray tomography**
Geophysics, 56 (1991), pp. 202-207
CrossRefView Record in Scopus

Worthington and Lubbe, 2007
M.H. Worthington, R. Lubbe**The scaling of fracture compliance**
Geol. Soc. Lond., Spec. Publ., 270 (2007), pp. 73-82
CrossRefView Record in Scopus

Wu and Toksoz, 1987
R.S. Wu, M.N. Toksoz**Diffraction tomography and multisource holography applied to seismic imaging**
Geophysics, 52 (1987), pp. 11-25
CrossRefView Record in Scopus

Zangerl et al., 2008
C. Zangerl, K. Evans, E. Eberhardt, S. Loew**Normal stiffness of fractures in granitic rock: a compilation of laboratory and in-situ experiments**
Int. J. Rock Mech. Min. Sci., 45 (2008), pp. 1500-1507
ArticleDownload PDFView Record in Scopus

Zheng et al., 2013
Y. Zheng, X. Fang, M.C. Fehler, D.R. Burns**Seismic characterization of fractured reservoirs by focusing Gaussian beams**
Geophysics, 78 (2013), pp. A23-A28
CrossRefView Record in Scopus